Understanding the reverse time migration backscattering: noise or signal?

Esteban Díaz and Paul Sava, Center for Wave Phenomena, Colorado School of Mines

SUMMARY

Reverse time migration (RTM) backscattered events are produced by the cross-correlation between waves reflected from sharp interfaces (e.g. the top of salt bodies). Commonly, these events are seen as a drawback for the RTM method because they obstruct the image of the geologic structure. Many strategies have been developed to filter out the artifacts from the conventional image. However, these events contain information that can be used to analyze kinematic synchronization between source and receiver wavefields reconstructed in the subsurface. Numeric and theoretical analysis indicate the sensitivity of the backscattered energy to velocity accuracy: an accurate velocity model maximizes the backscattered artifacts. The analysis of RTM extended images can be used as a quality control tool and as input to velocity analysis designed to constrain salt models and sediment velocity.

INTRODUCTION

Reverse time migration (RTM) is not a new imaging technique (Baysal et al., 1983; Whitmore, 1983; McMechan, 1983). However, it was not until the late 1990s that computational advances allowed the geophysical community to use this technology for exploratory 3D surveys. In complex geological settings, RTM produces better images than other methods.

A striking characteristic of RTM is the presence of low wavenumber events, uncorrelated with the geology, in models with sharp interfaces (e.g. salt intrusions). The seismic industry has dedicated effort and time developing algorithms and strategies to filter out the backscattered energy from the image. We can classify the filtering approaches in two general families: pre-imaging condition and post-imaging condition.

The pre-imaging condition family modifes the wavefields (either by modeling or by wavefield decomposition) such that the backscattered events do not form during the imaging process. One strategy is wavefield decomposition (Liu et al., 2011; Fei et al., 2010). In this method only wavefields propagating in opposite directions are cross-correlated. The modeling approach modifes the wavefields by not allowing waves to reflect during propagation. One way to achieve this is by introducing an absorbing boundary condition in the wave equation at the top of salt (Fletcher et al., 2005), or by impedance matching (Baysal et al., 1984).

In the post-imaging family, the artifacts are attenuated by filtering, which is a considerably cheaper process because operates in the image space and not on the much larger and more complex wavefields. A common strategy is to apply a Laplacian filter to the image (Youn and Zhou, 2001). Another option is a signal/noise separation by least-squares filtering (Guitton et al., 2007). One can also consider using extended images (Rickett and Sava, 2002; Sava and Fomel, 2006; Sava and Vasconcelos, 2011) for filtering. This method (Kaelin and Carvajal, 2011) takes advantage of the slope difference between primary and backscattered events in the time-lag gathers.

In this paper, we analyze the information carried by the backscattered energy in the extended images. We show that the backscattered waves provide important information about the synchronization between the reconstructed wavefields in the subsurface. The presence of backscattered energy in the image not only depends on the interpretation of the sharp interface but also on the velocity above it. We analyze the mapping patterns of the backscattered events in the extended images and conclude that backscattered energy is sensitive to the velocity model accuracy and therefore should be used as a source of information for migration velocity analysis (MVA). Counter to common practice, we assert that backscattering artifacts should be enhanced during RTM to constrain the velocity models, and they should only be removed in the last stage of imaging.

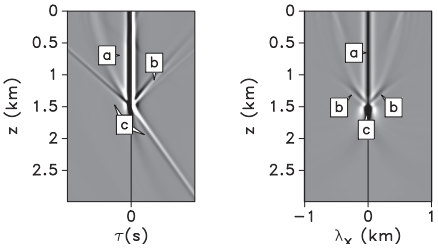

Figure 1: Synthetic example: (a) time-lag and (b) space-lag gathers at x=5km.

THEORY

The conventional imaging condition (CIC) (Claerbout, 1985) is a zero time-lag cross-correlation between the source wavefield and the receiver wavefields:

$$R(\mathbf{x}) = \sum_{shots} \sum_{t} W_s(\mathbf{x}, t) W_r(\mathbf{x}, t). \qquad (1)$$

A wavefield extrapolated with RTM could show, depending on the complexity of the geology, waves traveling in both upward and downward directions, such as diving waves, head waves and backscattered waves. The correlation between forward and backscattered waves is particularly strong when sharp boundaries are present in the velocity model (e.g. for salt bodies).

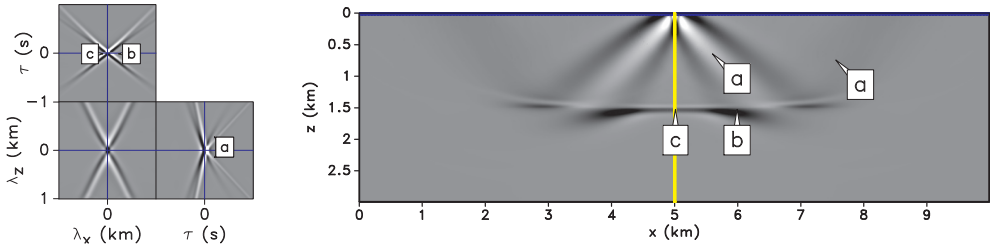

(a) (b)

Figure 2: Synthetic example: (a) common image point at $(x, z) = (5.0, 1.5)$km and (b) migrated image of one shot.

If a sharp boundary is present in the model, we can decompose the source wavefield into transmitted and reflected energy that originates at the sharp boundary:

$$W_s(\mathbf{x}, t) = W_s^r(\mathbf{x}, t) + W_s^t(\mathbf{x}, t), \tag{2}$$

where the superscripts t and r stand for transmitted and reflected energy, respectively. The same idea can be applied to the receiver wavefield:

$$W_r(\mathbf{x}, t) = W_r^r(\mathbf{x}, t) + W_r^t(\mathbf{x}, t). \tag{3}$$

By taking advantage of the linearity of equation 1, we can split the conventional imaging condition as follows:

$$R(\mathbf{x}) = R^{tt}(\mathbf{x}) + R^{rr}(\mathbf{x}) + R^{tr}(\mathbf{x}) + R^{rt}(\mathbf{x}). \tag{4}$$

Here, the first superscript is associated with the source wavefield and the second is associated with the receiver wavefield. For example, $R^{tr}(\mathbf{x})$ is an image constructed with the transmitted source wavefield and the reflected receiver wavefield.

This analysis can be used as well with the extended imaging condition (EIC) (Rickett and Sava, 2002; Sava and Fomel, 2006; Sava and Vasconcelos, 2011). The EIC is similar to the CIC except that the cross-correlation lags between source and receiver wavefields are preserved in the output as follows:

$$R(\mathbf{x}, \boldsymbol{\lambda}, \tau) = \sum_{shots} \sum_{t} W_s(\mathbf{x} - \boldsymbol{\lambda}, t - \tau) W_r(\mathbf{x} + \boldsymbol{\lambda}, t + \tau). \tag{5}$$

Here $\boldsymbol{\lambda}$ and τ represent the cross-correlation space-lags and time-lags, respectively. The conventional image is a special case of the extended image $R(\mathbf{x}) = R(\mathbf{x}, \mathbf{0}, 0)$.

By using extended images, we can measure the accuracy of the velocity model by analyzing the moveout of the events (Yang and Sava, 2010), and we can perform transformations from the extended to the angle domain (Sava and Fomel, 2003, 2006; Sava and Vlad, 2011). The extended images provide a measurement of the similarity between the source and receiver wavefields along space and time, so we can exploit these images to analyze the RTM backscattered events.

In the presence of sharp boundaries, we can also construct four partial extended images:

$$\begin{aligned} R(\mathbf{x}, \boldsymbol{\lambda}, \tau) = {} & R^{tt}(\mathbf{x}, \boldsymbol{\lambda}, \tau) + R^{rr}(\mathbf{x}, \boldsymbol{\lambda}, \tau) \\ & + R^{tr}(\mathbf{x}, \boldsymbol{\lambda}, \tau) + R^{rt}(\mathbf{x}, \boldsymbol{\lambda}, \tau). \end{aligned} \tag{6}$$

By analyzing the individual contributions to the image and extended image, we can better understand the behavior of the backscattered events. This analysis is similar to the one of Fei et al. (2010) and Liu et al. (2011) whose objective is to filter out the non-geological portions of the image. Here, we approach the problem in a broader sense by attempting to understand the physical meaning of the backscattered energy and its uses for velocity analysis.

In order to gain an understanding of the RTM backscattered events, we use a simple model with two-layers and a strong velocity contrast. Figure 2(b) shows the image obtained with the conventional imaging condition for one shot at $x = 5km$. This image has strong backscattered energy (indicated with letter "a") above the reflector located at $z = 1.5km$. Figures 1(a), 1(b) and 2(a) show a time-lag gather, a space-lag gather and a common image (CIP) point gather. The backscattered energy $R^{tr}(\mathbf{x}, \boldsymbol{\lambda}, \tau) + R^{rt}(\mathbf{x}, \boldsymbol{\lambda}, \tau)$ (denoted with letter "a") maps toward zero lag for time-lag and space-lag gathers, as shown in Figures 1(a) and 1(b), respectively. This mapping to zero lag means that the reflected wavefields map in perfect synchronization with the transmitted wavefields; therefore they cannot be dissociated in the imaging condition. This synchronization is achieved only because we use the correct velocity model to obtain these images. We can also identify the cross-correlation between the reflected wavefields (denoted by letter "b") in Figures 1(a) and 1(b) for time-lag and space-lag gathers, respectively. In the time-lag gathers, this event has an opposite slope compared with the one of the primaries, as if we changed the cross-correlation order in equation 5.

The backscattered events (identified with letter "a") also appear in CIP gathers, as shown in Figure 2(a). Both backscattered contributions map to $\tau > 0$ in the $\tau - \lambda_z$ plane. However, they map as two different events, whereas for time-lag and space-lag gathers both map to zero lag. In the $R^{tr}(\mathbf{x}, \boldsymbol{\lambda}, \tau)$ image, they map to $\tau > 0$ and $\lambda_z > 0$, and in the $R^{rt}(\mathbf{x}, \boldsymbol{\lambda}, \tau)$ image they map to $\tau > 0$ and $\lambda_z < 0$.

SENSITIVITY TO VELOCITY ERRORS

In this section, we test the dependency of the backscattered energy on velocity errors using extended images.

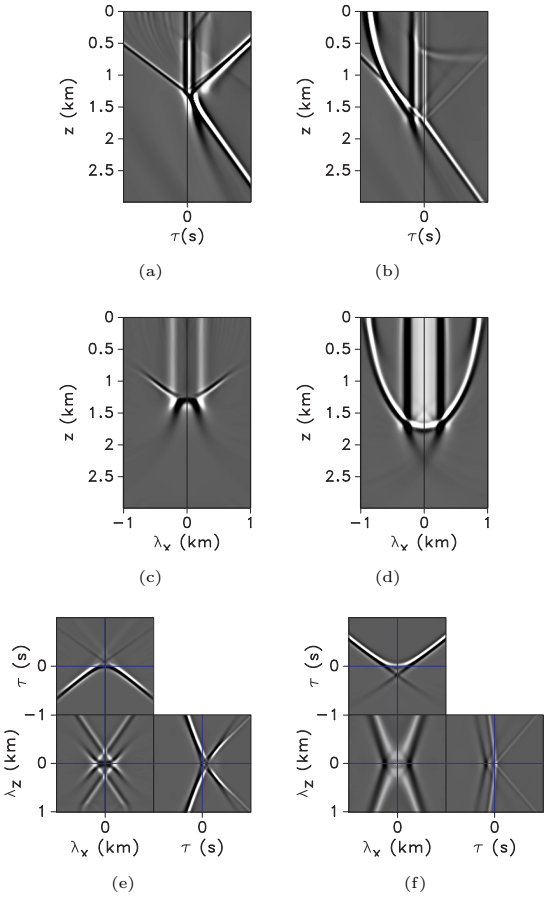

Figure 3: Sample gathers with -12% and +12% velocity error: (a)-(b) time-lag gathers, (c)-(d) space-lag gathers, (e)-(f) CIP gathers.

We analyze the behavior of backscattered events in the presence of velocity errors. We test the sensitivity of the backscattered events with the same synthetic data discussed previously. In this case, we construct the images with different models characterized by a constant error varying from -12% to +12% in layer 1. We keep the interface consistent with the velocity used for imaging, i.e. the interface producing backscattered energy is placed in the model according to the velocity in layer 1.

Figures 3(a) and 3(b) show time-lag gathers for a -12% and +12% velocity error, respectively. One can see that the backscattered energy does not map to $\tau = 0$ because the wavefields are no longer synchronized. For negative errors the artifacts map to $\tau > 0$, whereas for positive errors they map to $\tau < 0$. Figures 3(c) and 3(d) show space-lag gathers for the same velocity errors. In this case we see that the backscattered energy maps symmetrically away with respect to $\lambda_x = 0$. Figures 3(e) and 3(f) show CIP gathers for the same velocity errors. One can see that the velocity errors split the backscattered energy in the $\lambda_z - \tau$ and $\lambda_x - \lambda_z$ planes; some of the energy goes trough zero space-lag, while other part of the energy does not.

We can use the kinematic information from backscattered events contained in the extended images to design objective functions (OF) that exploit the presence of backscattered events. To isolate the backscattered events, we use wavefield decomposition to obtain the individual contributions shown in equation 6. We use the images $R^{tr}(\mathbf{x}, \boldsymbol{\lambda}, \tau)$ and $R^{rt}(\mathbf{x}, \boldsymbol{\lambda}, \tau)$ which contain backscattered energy. Minimizing such OF, e.g. by wavefield tomography, optimizes the sharp interface positioning (e.g. the top of salt) and the sediment velocity above it. A straightforward approach based on differential semblance optimization (Shen et al., 2003) can be adapted to use the backscattered energy seen away from zero lags by defining objective functions for time-lag gathers

$$J_\tau = \frac{1}{2}\|P(\tau)\left[R^{tr}(z,\tau) + R^{rt}(z,\tau)\right]\|_2^2, \qquad (7)$$

and for space-lag gathers,

$$J_{\lambda_x} = \frac{1}{2}\|P(\lambda_x)\left[R^{tr}(z,\lambda_x) + R^{rt}(z,\lambda)\right]\|_2^2. \qquad (8)$$

The functions $P(\tau) = |\tau|$ and $P(\lambda_x) = |\lambda_x|$ penalize the backscattered energy away from zero lags, thus defining the residual that we need to minimize trough inversion. For common image points we can use

$$J_{\mathbf{c}} = \frac{1}{2}\|P(\boldsymbol{\lambda}, \tau)\left[R^{tr}(\boldsymbol{\lambda},\tau) + R^{rt}(\boldsymbol{\lambda},\tau)\right]\|_2^2. \qquad (9)$$

The penalty functions are designed to measure the deviation error between actual and ideally focused extended images. For CIGs we have a definite criterion: we know that the backscattered energy has to map to zero lag. However, for CIPs the penalty operator is more complex. We use a correct CIP as reference for constructing the penalty function $P(\boldsymbol{\lambda}, \tau)$. The correct CIP, shown in Figure 2(a), has the correct focusing within the acquisition limitations. We could use a demigration/migration process to assess correct focusing at a given CIP position, and to infer the shape of the penalty operator, similar to the method proposed by Yang et al. (2012)

The objective functions for our synthetic example are shown in Figure 4 for time-lag CIGs, space-lag CIGs, and common image point gathers, respectively. In all three cases the OF minimizes at the correct model.

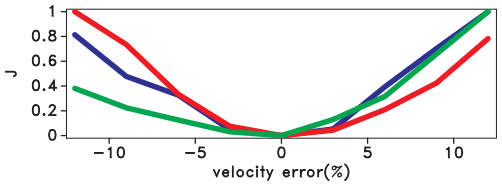

Figure 4: Normalized objective functions J_τ (red), J_{λ_x} (blue) and $J_{\mathbf{c}}$ (green).

EXAMPLE

In this section, we illustrate the backscattered events visible on extended images constructed with the Sigsbee 2A model (Paffenholz et al., 2002). We modify the

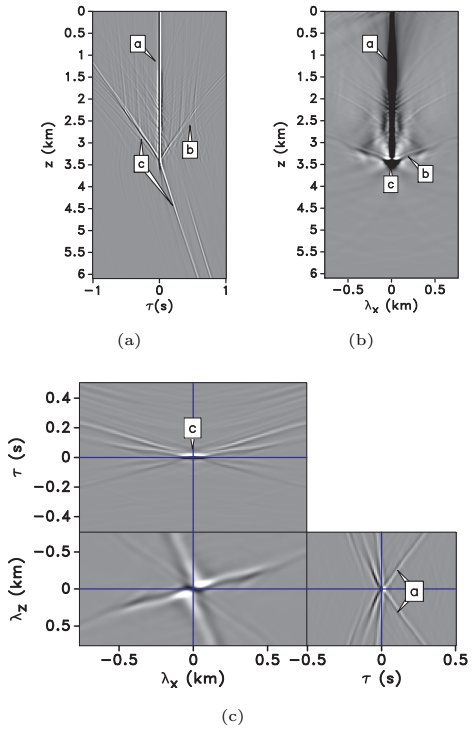

Figure 5: Sigsbee analysis: time-shift CIG (a) and space-lag CIG (b) at $x = 19.1km$, and a common image point gather at $(x, z) = (19.1, 3.45)$km (c).

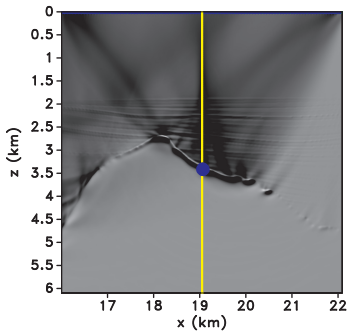

Figure 6: Sigsbee RTM image (d). The vertical line and blue dot show the CIG and CIP locations, respectively.

model by salt flooding (extending the salt to the bottom of the model) to avoid backscattering from the base of salt; therefore we focus on the reflections from the top of salt only. For this example we fix the receiver array on the surface, and we use 100 shots evenly distributed on the surface to build the image. For the migration model, we use the stratigraphic velocity which has sharp interfaces in the sediment section, in addition to the interface corresponding with the top of salt. Figure 6 shows the conventional image for our modified Sigsbee model; note the strong backscattered energy above the salt.

Figure 5(a) shows a time-lag gather calculated at $x = 19km$. We can see that the gather is very complex, but we can easily identify the backscattered energy (indicated with letter "a") in Figure 5(a). In this case, the backscattered energy maps directly to $\tau = 0$ because we use the correct velocity model. We can also identify the events corresponding to the cross-correlation between reflected waves from the source and receiver side $R^{rr}(z, \tau)$, (indicated with letter "b"). The $R^{rr}(z, \tau)$ events have positive slope (given by the sediment velocity at the interface) and are visible for $\tau > 0$. We can also observe an abrupt change in the slope of the primary reflection corresponding to the sediment-salt interfaces at the top of salt, (indicated with letter "c").

Figure 5(b) shows a space-lag common image gather extracted at the same location. The backscattered energy maps toward $\lambda_x = 0$ (indicated with letter "a"). We see again the $R^{rr}(z, \lambda_x)$ case (indicated with letter "b") where the energy is mapped away from zero lag. Even though we are using the correct model, we still see energy away from $\lambda_x = 0$. This indicates that additional processing is needed before we can use space-lag gathers for model update with wave equation tomography.

Figure 5(c) shows a common image point extracted at the top of the salt interface at $(x, z) = (19.05, 3.4)km$. Despite the complexity of this image, we can still identify similar patterns to the ones seen in the synthetic example, shown in Figure 2(a). The backscattered events are mapped to $\tau > 0$ in the $\tau - \lambda_z$ plane (indicated with letter "a"). In this plane, we can separate the individual contributions from $R^{tr}(\mathbf{x}, \boldsymbol{\lambda}, \tau)$ (which maps to $\lambda_z < 0$ and $\tau > 0$) and $R^{rt}(\mathbf{x}, \boldsymbol{\lambda}, \tau)$ (which maps to $\lambda_z > 0$ and $\tau > 0$) because they are imaged into two different events. In the common image gathers discussed before, we cannot differentiate the individual contributions because both events map to zero lag. The reflection maps as a point to zero lag in the $\tau - \lambda_x$ plane (indicated with letter "c").

CONCLUSIONS

RTM backscattered events map to zero lag in the extended images when the velocity is correct. This means that the reflected receiver wavefield travels in perfect synchronization with the source wavefield and vice versa. We demonstrate that the RTM backscattered energy is sensitive to kinematics errors in the velocity model. The backscattered energy should be maximized in the image in order to ensure an optimum velocity model. The analysis of backscattered energy on extended images provides a definite criterion to update velocity models with salt interfaces (i.e in the Gulf of Mexico). Further tests are needed to develop automated velocity model update based on the maximization of the backscattered energy.

ACKNOWLEDGMENTS

This work was supported by the sponsors of the Center for Wave Phenomena at Colorado School of Mines. The reproducible numeric examples in this paper use the Madagascar open-source software package freely available from http://www.reproducibility.org.

REFERENCES

Baysal, E., D. D. Kosloff, and J. W. C. Sherwood, 1983, Reverse time migration: Geophysics, **48**, 1514–1524.

———, 1984, A two-way nonreflecting wave equation: Geophysics, **49**, 132–141.

Claerbout, J. F., 1985, Imaging the earth's interior: Blackwell Scientific Publications, Inc.

Fei, T. W., Y. Luo, and G. T. Schuster, 2010, Deblending reverse-time migration: SEG Technical Program Expanded Abstracts, **29**, 3130–3134.

Fletcher, R. F., P. Fowler, P. Kitchenside, and U. Albertin, 2005, Suppressing artifacts in prestack reverse time migration: SEG Technical Program Expanded Abstracts, **24**, 2049–2051.

Guitton, A., B. Kaelin, and B. Biondi, 2007, Least-squares attenuation of reverse-time-migration artifacts: Geophysics, **72**, S19–S23.

Kaelin, B., and C. Carvajal, 2011, Eliminating imaging artifacts in rtm using pre-stack gathers: SEG Technical Program Expanded Abstracts, **30**, 3125–3129.

Liu, F., G. Zhang, S. A. Morton, and J. P. Leveille, 2011, An effective imaging condition for reverse-time migration using wavefield decomposition: Geophysics, **76**, S29–S39.

McMechan, G. A., 1983, Migration by extrapolation of time-dependent boundary values: Geophysical Prospecting, **31**, 413–420.

Paffenholz, J., B. McLain, J. Zaske, and P. Keliher, 2002, Subsalt multiple attenuation and imaging: Observations from the sigsbee 2b synthetic dataset: 72nd Annual International Meeting, SEG, Expanded Abstracts, 2122–2125.

Rickett, J. E., and P. C. Sava, 2002, Offset and angle-domain common image-point gathers for shot-profile migration: Geophysics, **67**, 883–889.

Sava, P., and S. Fomel, 2006, Time-shift imaging condition in seismic migration: Geophysics, **71**, S209–S217.

Sava, P., and I. Vasconcelos, 2011, Extended imaging conditions for wave-equation migration: Geophysical Prospecting, **59**, 35–55.

Sava, P., and I. Vlad, 2011, Wide-azimuth angle gathers for wave-equation migration: Geophysics, **76**, S131–S141.

Sava, P. C., and S. Fomel, 2003, Angle-domain common-image gathers by wavefield continuation methods: Geophysics, **68**, 1065–1074.

Shen, P., W. W. Symes, and C. C. Stolk, 2003, Differential semblance velocity analysis by wave-equation migration: SEG Technical Program Expanded Abstracts, **22**, 2132–2135.

Whitmore, N. D., 1983, Iterative depth migration by backward time propagation: SEG Technical Program Expanded Abstracts, **2**, 382–385.

Yang, T., and P. Sava, 2010, Moveout analysis of wave-equation extended images: Geophysics, **75**, S151–S161.

Yang, T., J. Shragge, and P. C. Sava, 2012, Illumination compensation for image-domain wavefield tomography: SEG annual meeting 2012, SUBMITTED, **1**.

Youn, O. K., and H. Zhou, 2001, Depth imaging with multiples: Geophysics, **66**, 246–255.